

PAPER

View Article Online
View Journal | View Issue



Cite this: Nanoscale, 2025, 17, 17745

# Nanostructuring copper thin film electrodes for $CO_2$ electroreduction to $C_{2+}$ products†

Dimitra Papamichail, D<sup>a</sup> Filippo Franceschini, D<sup>b</sup> Imran Abbas, D<sup>a</sup> Deema Balalta, D<sup>c</sup> Trang Thi Hong Nguyen, D<sup>a</sup> Deepak Pant, D<sup>c</sup> Sara Bals, D<sup>c</sup> Irene Taurino, D<sup>c</sup> Ewald Janssens, D<sup>c</sup> Didier Grandjean D<sup>c</sup> and Peter Lievens D<sup>a</sup>

The electrochemical CO<sub>2</sub> reduction reaction (CO<sub>2</sub>RR) is a promising approach for achieving carbonneutral processes in the chemical industry. In this context, various nanostructures have been reported to enhance the C<sub>2+</sub> selectivity of Cu-based catalysts. Here, we prepared Cu nanoneedles (NN) from 300 nm sputtered Cu thin films through anodization under various conditions and investigated their performance in terms of  $C_{2+}$  product selectivity. Various combinations of anodization potentials (+0.75  $V_{RHF}$ , +0.85  $V_{RHE}$ , and  $+0.95~V_{RHE}$ ) and KOH electrolyte concentrations (0.1 M, 0.5 M and 1.0 M) allow the tailoring of the NN length and density that are linked to their CO<sub>2</sub>RR product selectivity at -1.0 V<sub>RHE</sub>. The best performance using the  $C_{2+}$ :  $C_1$  ratio was achieved with a high NN surface density. A detailed analysis using high-angle annular dark-field scanning transmission electron microscopy and X-ray absorption fine structure spectroscopy of the best performing sample shows that the anodization of a Cu thin film produces NNs composed of a uniform 3D network of 2 nm hydroxide nanoparticles (NPs) and reconstructs into a rougher metallic Cu NP network after the CO<sub>2</sub>RR. A high density of NNs with this inner structure may lead to an increase in the local CO concentration and thus to  $C_{2+}$  products. This systematic work demonstrates that nanostructuring the surface of copper thin film electrodes can enhance the CO<sub>2</sub>RR selectivity to C<sub>2+</sub> products while the correlation between the NN morphology and their inner structure strengthens further their applications as CO2 electrocatalysts.

Received 14th April 2025, Accepted 29th June 2025 DOI: 10.1039/d5nr01514f

rsc.li/nanoscale

#### Introduction

The electrochemical  $\mathrm{CO_2}$  reduction reaction ( $\mathrm{CO_2RR}$ ) is a promising emerging technology to mitigate the increase in anthropogenic carbon dioxide levels responsible for global climate change. Coupled with renewable energy, the electrochemical conversion of  $\mathrm{CO_2}$  in aqueous media can produce valuable fuels and chemicals that are conventionally derived

So far, the optimal binding energy for adsorbed CO (\*CO) is a unique feature of Cu and is thought to enable the formation of multicarbon products, especially  $C_{2+}$ .<sup>5</sup> However, despite extensive research and technological advances of the state-of-the-art Cu-based CO<sub>2</sub>RR catalysts,<sup>6</sup> their insufficient selectivity and poor stability remain important challenges. Better control over the \*CO intermediate may allow unlocking the selectivity of chemical pathways to  $C_{2+}$  products which could aid in the design of improved materials.<sup>7</sup>

Recently, nanostructuring of copper surfaces has been introduced as an efficient method to favour the formation of  $C_{2+}$  over  $C_1$  products. In particular, Cu-derived (Cu(OH)<sub>2</sub> or CuO) nanoneedle (NN) structured electrodes feature a significant enhancement in  $C_{2+}$  product formation, while their faradaic efficiency (FE) for methane formation is minimized to less than 1%, allowing an efficient separation of  $C_1$  and  $C_{2+}$  products. This remarkable selectivity improvement has been attributed to the force-field effect created by the high-curved structures of NNs that can accommodate a higher number of hydrated cations. Their pres-

ewald.janssens@kuleuven.be

from petroleum processes. $^{1-3}$  Among them  $C_{2+}$  products and in particular ethylene are the most desired molecules by industry. The latter molecule features a high energy density and is an important precursor in many industrial processes. $^4$ 

<sup>&</sup>lt;sup>a</sup>Quantum Solid State Physics, Department of Physics and Astronomy, KU Leuven, 3001 Leuven, Belgium. E-mail: didier.grandjean@kuleuven.be,

<sup>&</sup>lt;sup>b</sup>Semiconductor Physics, Department of Physics and Astronomy, KU Leuven, 3001 Leuven, Belgium

 $<sup>^</sup>c$ Electron Microscopy for Materials Science (EMAT), University of Antwerp, 2020 Antwerp, Belgium

<sup>&</sup>lt;sup>d</sup>Micro and Nano Systems (MNS), Department of Electrical Engineering (ESAT), KU Leuven, 3001 Leuven, Belgium

<sup>&</sup>lt;sup>e</sup>Electrochemistry Excellence Centre, Flemish Institute for Technological Research

<sup>(</sup>VITO), 2400 Mol, Belgium

<sup>f</sup>Center for Advanced Process Technology for Urban Resource Recovery (CAPTURE),
Frieda Saevsstraat 1. 9052 Zwijnaarde. Belgium

<sup>†</sup> Electronic supplementary information (ESI) available. See DOI: https://doi.org/10.1039/d5nr01514f

ence seems crucial in promoting the hydrocarbon selectivity as partment ce demonstrated by Monteiro *et al.*<sup>10</sup> However, the exact nature of concentration the active sites on oxide derived Cu is still deboted. Some

demonstrated by Monteiro *et al.*<sup>10</sup> However, the exact nature of the active sites on oxide-derived Cu is still debated. Some propose that dual  $\text{Cu}^{\delta+}$ – $\text{Cu}^0$  sites<sup>11–15</sup> participate in the enhancement of  $\text{C}_{2+}$  product selectivity. According to other studies, the reduction of copper to  $\text{Cu}^0$  always precedes the  $\text{CO}_2\text{RR}$ , <sup>16–18</sup> with a recent study highlighting the important role of the metal particle size in boosting  $\text{C}_{2+}$  production. <sup>16</sup>

Cu NNs can be formed chemically<sup>19</sup> or more conveniently through the anodization of a metal plate, usually in an alkaline solution,  $^{20,21}$  with few works using bicarbonate electrolytes.  $^{22}$  The anodization regime offers a versatile, fast, and economical way to nanostructure metallic surfaces, including copper. The self-organizing process allows for the growth of nanostructured mixed  $\text{Cu}(\text{OH})_2$  and  $\text{Cu}(\text{OH})_2$  phases that increase the original metal surface area by several orders of magnitude.

The utilization of thin films produced by physical vapor deposition methods has been proven to be very appealing for industrial catalysis applications, 23-26 such as gas diffusion electrodes that are used in electrolyzers. Compared to conventional bulk foils, their film fabrication combines a better control over the film thickness with a higher flexibility regarding the type of substrate. Nonetheless, the specific morphological changes induced by their reconstruction under electrochemical treatments have not been explored in depth. The growth of NNs via the anodization of a Cu electrode is usually controlled by the applied potential or current, the electrolyte concentration and the pH used.27,28 Typically, a high current density or potential is applied in a highly concentrated KOH electrolyte to develop the NN structures. 8,29,30 However, neither a rational justification of the applied conditions nor a systematic investigation of the link between the NN structure/morphology and its CO<sub>2</sub>RR selectivity has been given.

In this study, the relationship between the potentiostatic anodization conditions of copper thin films and the resulting NNs' morphology, length and density as well as their respective ethylene or  $C_{2+}$  selectivity in the  $CO_2RR$  is investigated. Preand post-reaction characterization of the best-performing NN electrode using a combination of electron microscopy and X-ray emission and absorption spectroscopy allows further understanding of the structural origin of its  $CO_2RR$  selectivity. The results of this work will contribute to a more rational design of selective  $CO_2RR$  electrocatalysts.

## 2. Experimental methods

#### 2.1. Synthesis of copper electrodes

Cu/Pt/glass (99.99%, Neyco/Schott Benelux) electrodes were fabricated using radiofrequency (RF) sputtering following the procedure described in ref. 31. Using Kapton tape, the geometric area of the electrodes was determined to be  $0.7 \times 0.7$  cm<sup>2</sup>.

#### 2.2. Electrochemical experiments

**2.2.1. Anodization of copper thin films.** The anodization experiments were conducted in a three-electrode single com-

partment cell. The KOH ( $\geq$ 85%, pellets, ACS reagent, Fluka) concentration of the electrolyte was varied in a range from 0.1 to 1.0 M. All the electrolytes were diluted to the required concentrations by mixing them with Milli-Q water (18.2 M $\Omega$  cm). For the anodization process, a Hg/HgO (1.0 M KOH) reference electrode (RE) and a Pt gauze (2.25 cm²) counter electrode (CE) were used. Applied potentials were measured with respect to the Ag/AgCl and Hg/HgO REs and converted to the reversible hydrogen electrode (RHE) scale:

$$E_{\text{RHE}} = E_{\text{(Ag/AgCl, KCl 3.4 M)}} + E_{\text{(Ag/AgCl, KCl 3.4 M)}}^{\circ} + 0.059 \,\text{pH}$$
 (1)

$$E_{\text{RHE}} = E_{\text{(Hg/HgO, KOH 1 M)}} + E_{\text{(Hg/HgO, KOH 1 M)}}^{\circ} + 0.059 \,\text{pH}$$
 (2)

where  $E_{\rm RHE}$  is the converted potential *versus* the reversible hydrogen electrode, RHE,  $E_{\rm (Ag/AgCl,\ KCl\ 3.4\ M)}$  is the measured potential against the Ag/AgCl (KCl 3.4 M) reference electrode, and  $E_{\rm (Ag/AgCl,\ KCl\ 3.4\ M)}^{\circ}$  is the standard potential of Ag/AgCl at 25 °C (0.205 V<sub>SHE</sub>). The same applies for the Hg/HgO RE with  $E_{\rm (Hg/HgO,\ KOH\ 1\ M)}^{\circ}$  at 25 °C (0.098 V<sub>SHE</sub>). Unless otherwise specified, potentials reported hereafter are given  $\nu s$ . RHE (V<sub>RHE</sub>).

The measurement protocol starts with cyclic voltammetry (CV) in the -0.15 – +1.5  $V_{RHE}$  potential window using a scan rate of 100 mV s<sup>-1</sup> to identify the Cu redox peaks. For each anodization, a fresh Cu electrode was used and was polarized at -0.1  $V_{RHE}$  for 50 s to reduce the thickness of the native surface oxide layer, before the application of oxidative potentials of +0.75  $V_{RHE}$ , +0.85  $V_{RHE}$  and +0.95  $V_{RHE}$  for 150 s. Each applied potential results in a different electrode. After anodization, the electrode was rinsed with Milli-Q water and dried under  $N_2$ .

2.2.2. Electrochemical CO<sub>2</sub> reduction. The electrochemical experiments were carried out in a gas-sealed H-cell controlled from an electrochemical potentiostat (CS2350 bipotentiostat, Corrtest Instruments). The two compartments were separated by a cation exchange membrane (117-Nafion). A leak-free Ag/ AgCl 3.4 M KCl (LF-1.6, Innovative Instruments, Inc.) was used as the RE and a Pt gauze  $(2.25 \text{ cm}^2)$  as the CE.  $CO_2$  saturated-0.1 M KHCO<sub>3</sub> with pH 6.8 ( $\geq$ 99.7%, p.a., ACS, Carl Roth) (7 ml, 3 ml headspace) and 1.0 M KOH (6 ml) electrolyte solutions were used in the cathodic and anodic compartments, respectively. Before the CO<sub>2</sub>RR, the catholyte was bubbled with CO<sub>2</sub> for 40 min and stirred with a magnetic stirrer at a constant rate of ~500 rpm. For the electrolysis, a CO2 flow rate (4.8 grade, Air Liquide) of 5 ml min<sup>-1</sup> was used. Electrochemical impedance spectroscopy (EIS) was used to measure the uncompensated resistance  $R_{\rm u}$  (where  $Z_i$  is 0) of the electrochemical system at a potential of  $-1.0\ V_{RHE}$  in the frequency range  $4 \times 10^5$ –1 Hz. The  $R_{\rm u}$  value was used in the post-iR correction as given by  $E = E_{RHE} - iR_{U}$ .

Gaseous products were analysed with a gas chromatograph (GC, Trace 1300, Thermo Fisher Scientific) using a sampling interval of 12 min. At the end of each experiment, 3 ml of electrolyte was stored in a refrigerator to preserve the volatile compounds. An Agilent 1200 high-performance liquid chromato-

Nanoscale Paper

graphy system with an Agilent Hi-Plex H 7.7 × 300 mm column was used to separate the product, and an Agilent 1260 RID detector was used to detect and quantify formate in the form of formic acid. The samples were previously diluted with water or a mobile phase. Here 0.01 M H<sub>2</sub>SO<sub>4</sub> was used as the mobile phase. Organic products concentrations (i.e. ethanol, propanol and acetaldehyde) were measured using headspace-GC combined with an FID and MS detector. The compounds were separated on a DB-WAXetr column 60 m  $\times$  0.25 mm  $\times$  0.25  $\mu m$ . Vials were heated in a closed headspace vial and the headspace was injected into the GC. A specific temperature profile was used to separate the several alcohols. The faradaic efficiencies (FE) of the different products were calculated using:

$$FE_{i,gas}(\%) = Q_{exp,i}/Q_{total} = (z_i \times n_i \times F)/(I \times t), \tag{3}$$

$$FE_{i \text{ liquid}} = (c \times V \times n_i \times F) / (M_w \times I \times t), \tag{4}$$

where  $Q_{\exp,i}$  is the amount of charge consumed for product i,  $Q_{\text{total}}$  is the total accumulated charge, F is the Faraday constant (96 485 C mol<sup>-1</sup>),  $z_i$  is the number of exchanged electrons for each specific product, and  $n_i$  is the number of moles of product i.  $Q_{\text{total}}$  is the product of applied current (I) and experiment duration (t), c is the concentration of liquid products, Vis the volume of the electrolyte, and  $M_{\rm w}$  is the molar mass of certain liquid products.

Before CO<sub>2</sub> electrolysis, linear sweep voltammetry (LSV) curves were recorded from 0 to -1.0 V<sub>RHE</sub> at a scan rate of 25 mV s<sup>-1</sup>. Chronoamperometry (CA) was performed at -1.0 V<sub>RHE</sub> for 1 h. The LSV and CA curves are shown in Fig. S3<sup>†</sup>. For the total FE estimation, the first 12 min are not included since the system had not reached steady-state in the H-cell (Fig. S4a†). The reported FE values results from three independent experiments. At the end of the experiment the electrolyte pH after the CO<sub>2</sub>RR was 7.3.

#### 2.3. Materials characterization

- 2.3.1. X-ray diffraction (XRD). The crystal structure of the synthesized materials was characterized by X-ray diffraction (X'Pert PRO MRD system) using Cu Kα radiation with a 1.5405 Å wavelength at a current of 40 mA and voltage of 50 kV. The scanning rate was  $2^{\circ}$  per min and the  $2\theta$  angle ranged from 10 to  $80^{\circ}$ .
- 2.3.2. Scanning electron microscopy (SEM). Micrographs of the AN-(x, y) electrodes were obtained by SEM using a FEI Helios Nanolab G3 CX DualBeam FIB/SEM with an acceleration voltage of 10 kV and an electron beam current of 86 pA.
- 2.3.3. X-ray photoelectron spectroscopy (XPS). The chemical stoichiometry and oxidation states of Cu and O were studied with X-ray photoelectron spectroscopy (XPS). XPS measurements were performed in a home-built setup at room temperature using Mg Ka X-rays (XR4 twin anode X-ray source, non-monochromatic) and an Alpha 110 hemispherical analyser. The spectra were acquired in ultra-high vacuum (UHV) (base pressure  $\sim 10^{-8}$  mbar) with an energy step of 0.1 eV, an energy resolution of ≈1 eV, and a beam diameter of 5 mm. The

recorded spectra were corrected by using the adventitious carbon peak C 1s at 284.8 eV.

- 2.3.4. X-ray absorption spectroscopy (XAS). Measurements were carried out at the XAFS beamline<sup>32</sup> of the Elettra synchrotron (Trieste, Italy) equipped with a Si (111) double crystal monochromator and water-cooled Pt-coated silicon mirrors which ensured higher order harmonic rejection. The X-ray absorption near edge spectroscopy (XANES) and extended X-ray absorption fine structure (EXAFS) of the electrodes at the Cu K-edge (8979 eV) were collected under ambient conditions in fluorescence detection mode using a silicon drift detector (SDD) and the incoming beam was measured using a nitrogenfilled ion chamber. The energy calibration was performed using the absorption spectrum of a metallic Cu foil. The XAS data were recorded up to a wavenumber of 12  $\mathring{A}^{-1}$ , with each spectrum taking approximately 30 minutes. At least two spectra were averaged to improve the signal to noise ratio. The background and normalization were carried out by fitting a straight line for the pre-edge and cubic spline, simulating the absorption of an isolated atom, for the post edge.
- 2.3.5. High-angle annular dark-field scanning transmission electron microscopy (HAADF STEM) and energy dispersive X-ray spectroscopy (EDS). The measurements were performed using an aberration-corrected cubed ThermoFisher Scientific Titan transmission electron microscope, operated at an accelerating voltage of 300 kV. The instrument was equipped with a Super X EDS detector. HAADF STEM was carried out ex situ after the anodization and the CO2RR by scratching the electrode surface, sonicating the detached material in ethanol, and drop casting the suspension on ultrathin film (UTF) carbon coated Au TEM grids. TEM lamellas were prepared using a Helios 5 Hydra UX plasma focused ion beam (PFIB) DualBeam system (Thermo Fisher Scientific Inc.)

#### 3. Results and discussion

#### 3.1. Anodization of sputtered copper electrodes

A series of magnetron sputtered 300 nm Cu thin films on glass substrates, Cu300, were anodized in various KOH concentrations and under different potentials to tailor their morphology.

Potentiostatic anodization was chosen over galvanostatic to explore the anodization of copper electrodes at specific potentials and to have the complete control over the reactions happening at the surface. To determine the optimal oxidation potential, CV was performed from +1.5 to -0.15 V<sub>RHE</sub> using a scan rate of 100 mV s<sup>-1</sup> at KOH electrolyte concentrations of  $c_{\text{KOH}} = 0.1 \text{ M}, 0.5 \text{ M}$  and 1.0 M, as shown in Fig. 1a. The cathodic peaks C and D are specific for the reduction of the oxidized species Cu2+ and Cu+ to Cu0, respectively. The oxidation peak A in the anodic sweep corresponds to Cu oxidation into Cu<sub>2</sub>O, i.e.  $Cu^0 \rightarrow Cu^+$ , while peak B is characteristic of  $Cu^+$  and/or  $Cu^0$  $\rightarrow$  Cu<sup>2+</sup> oxidation.

Peak B splits into two subpeaks, B<sub>1</sub> and B<sub>2</sub>. Notably, the former corresponds to the formation of Cu(OH)<sub>2</sub> and the latter

Paper Nanoscale

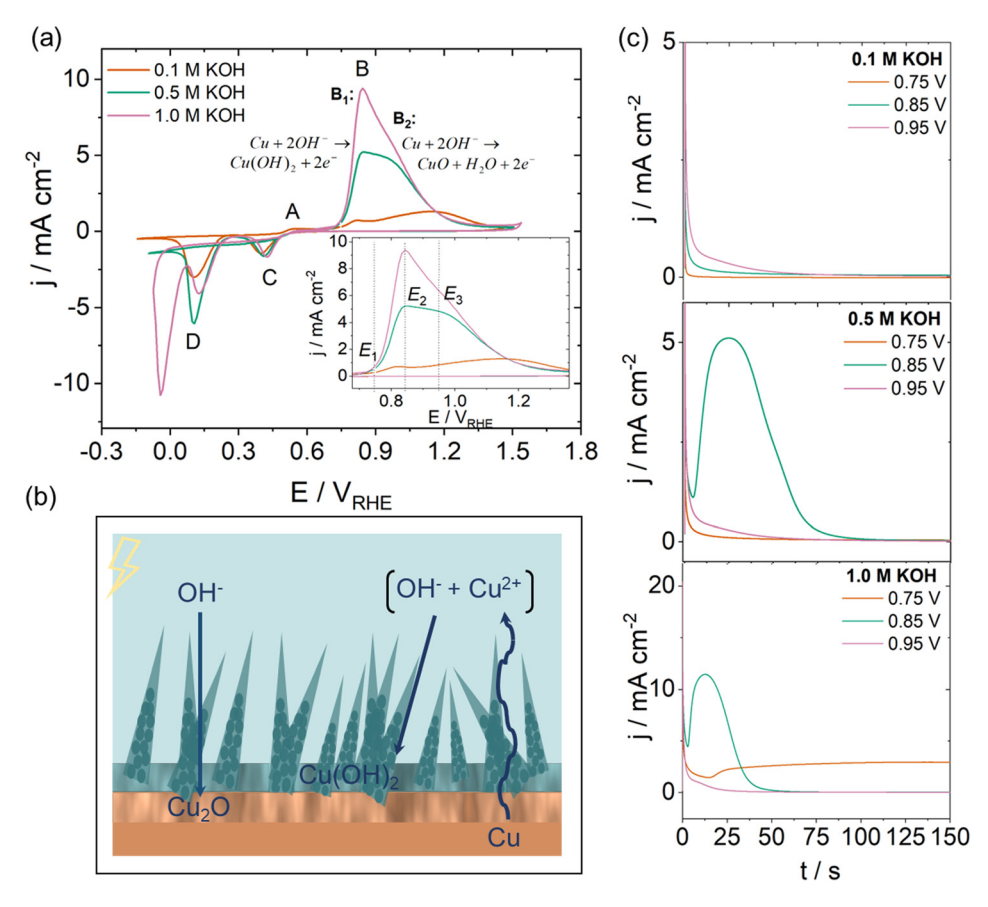


Fig. 1 (a) Cyclic voltammograms of the sputtered Cu electrodes,  $Cu_{300}$ , in 0.1 M, 0.5 M and 1.0 M KOH for the potential window between -0.15 and 1.5  $V_{RHE}$ , recorded at a scan rate of 100 mV s<sup>-1</sup>. Inset:  $Cu^{2+}$  oxidation region, peaks  $B_1$  and  $B_2$ . The vertical dotted lines represent the selected anodization potentials  $E_1$ ,  $E_2$  and  $E_3$ . (b) Schematic representation of the anodization process for Cu sputtered film,  $Cu_{300}$ . The straight arrows represent the interaction of species, *i.e.* Cu and  $Cu^{2+}$  with  $OH^-$  to give oxidation products, and the wavy arrow depicts the dissolution of Cu metal to  $Cu^{2+}$ . (c) Transient *j vs. t* curves for the different  $E_{an}$  potentials in 0.1, 0.5, and 1.0 M KOH for 150 s.

to CuO oxidation products, as given by the following chemical reactions:<sup>21,33</sup>

$$Cu + 2OH^{-} \rightarrow Cu(OH)_{2} + 2e^{-}$$
 (5)

$$Cu + 2OH^{-} \rightarrow CuO + H_2O + 2e^{-}$$
 (6)

Three anodization potentials ( $E_{\rm an}$ ) were selected based on the B peak of this CV response and are indicated by the dashed lines in the inset of Fig. 1a. Considering the specific reactions, *i.e.* (1) and (2), taking place at potentials close to B<sub>1</sub> and B<sub>2</sub> peaks, the electrode's morphology can be altered. Therefore, the potentials selected to investigate the growth of NNs are located before peak B<sub>1</sub> ( $E_1$  = 0.75 V<sub>RHE</sub>), around B<sub>1</sub> ( $E_2$  = 0.85 V<sub>RHE</sub>) and close to B<sub>2</sub> ( $E_3$  = 0.95 V<sub>RHE</sub>) to explore the region of NN formation and to optimize their shape (inset Fig. 1a).

According to Shoesmith *et al.*<sup>34</sup> the anodization starts with the formation of an initial  $Cu_2O$  layer as described by reaction (7). As this porous layer develops, metal dissolution in the form of  $Cu^{2+}$  occurs given by reaction (8). Since the pores get wider with time, some dissolution of  $Cu_2O$  must also take place according to reaction (9).

$$2Cu+2OH^-\rightarrow Cu_2O+H_2O+2e^- \eqno(7)$$

$$Cu + nOH^{-} \rightarrow (Cu(OH)_{n})^{2-n} + 2e^{-}$$
 (8)

$$Cu_2O + H_2O + (2n - 2)OH^- \rightarrow 2(Cu(OH)_n)^{2-n} + 2e^-$$
 (9)

$$\left(\operatorname{Cu}(\operatorname{OH})_{4}\right)^{2^{-}} \leftrightarrow \operatorname{Cu}(\operatorname{OH})_{2} + 2\operatorname{OH}^{-} \tag{10}$$

Although the anodization process is not fully understood yet, it is generally claimed to be governed by the dissolution processes of soluble  $(Cu(OH)_4)^{2-}$  complexes.<sup>35</sup> The build-up of  $(Cu(OH)_4)^{2-}$  near the electrode surface can lead to the nucleation and growth of insoluble  $Cu(OH)_2$  crystals through reaction (10). A schematic of the NN growth is shown in Fig. 1b.

The transient responses of current density j–t, depicted in Fig. 1c, can provide a mechanistic insight into the anodization process. Specifically, an initial drop in current density is observed across all KOH concentrations and anodization potentials. In the j–t curves, the timing of the drop varies, and the fastest drop is observed at 0.85  $V_{\rm RHE}$ , followed by later drops at 0.75  $V_{\rm RHE}$  and 0.95  $V_{\rm RHE}$ . The observed drop is likely due to the formation of a  $Cu_2O$  insulating layer resulting in an

Nanoscale Paper

increase of the charge transfer resistance of the electrode-electrolyte interface. The variation in time may reflect differences in the number of NN nuclei. The ascending current density is most pronounced for 0.85 V<sub>RHE</sub> in 0.5 and 1.0 M KOH and for 0.75 V in 1.0 M KOH. No current increase is seen for the 0.1M KOH-series and for 0.95 V<sub>RHE</sub> at 0.5 and 1.0 M KOH. This current increase translates into the nucleation and growth of the upper layer of  $(Cu(OH)_4)^{2-}$  resulting from the native oxide layer dissolution. Once the dissolution of these species starts, channels where fresh Cu is accessible to be dissolved further are available. Gradual supersaturation of  $(Cu(OH)_4)^{2-}$  causes Cu(OH)<sub>2</sub> to grow into a nanoneedle-like structure as indicated by the maximum value reached by the current. 18 As the Cu (OH)<sub>2</sub> crystals start to overlap and to cover the surface, partial passivation takes place and the current declines. Moreover, depending on the applied  $E_{\rm an}$  the colour of the Cu surface changes from luminous salmon red to darker tones indicating the successful creation of anodization products on the surface (Fig. S1†).

#### 3.2. Effect of $c_{KOH}$ and $E_{an}$ on the Cu NN structure

For convenience, the anodized copper electrodes will be referred to as AN-(x, y) where x is the applied potential and y the molarity of KOH in M used for the anodization. Depending on the anodization conditions, distinct Cu NN morphologies compared to that of planar Cu300 film can be identified through SEM in Fig. 2a. Although NNs are present for the lower 0.1 M concentrations at 0.85 and 0.95 V<sub>RHE</sub>, their growth is limited due to the insufficient supply of OH-. Significant higher coverages of NNs are observed on the electrode surface when the electrolyte concentration is increased to 0.5 M and especially to 1.0 M. For this reason, thorough characterization was performed for the full set of  $c_{KOH} = 0.5$  and 1.0 M at 0.75  $V_{RHE}$ . For AN-(0.75, 0.5), the density of the formed NNs is low and a significant fraction of the porous Cu<sub>2</sub>O layer is exposed. With respect to the j-t transient curves, the low-density morphology can be explained by the transport of Cu<sup>2+</sup> species from the dissolution sites to the crystal-growth sites. If the metal dissolution is facilitated, supersaturation of soluble Cu<sup>2+</sup> complexes occurs at the electrode surface leading to fast nucleation and growth of long NNs (average length of 3 ± 1 μm).

Although the NN morphology strongly relies on the applied  $E_{\rm an}$ , the current density can also provide information about their growth. Since the electrolyte concentration is relatively low (0.5 M), a low number of NN nucleation sites are formed explaining the inhomogeneous covering of the surface. The AN-(0.85, 0.5) electrode is characterized by a more homogeneous morphology with a high density of shorter NNs (average length of  $0.7 \pm 0.2 \, \mu \text{m}$ ). At high overpotentials, there is a rapid increase in the number of nucleation sites leading to a fast surface coverage inhibiting the metal dissolution and resulting in the growth of smaller crystals. Electrode AN-(0.95, 0.5) has only a few NNs grown horizontally on a roughened substrate. This condition falls in the passivation region that allows for a spontaneous oxidation of the Cu<sub>2</sub>O layer to CuO

preventing the NN formation. In AN-(0.75, 1) synthesized at the highest 1.0 M KOH concentration, a very distinct morphology with long bundles of NNs of a few micrometres ( $\sim$ 2.7 µm) growing in different directions on the electrode is found. Recall that the j(t) transient of AN-(0.75, 1) reached a steady-state with a constant current density of 3 mA cm<sup>-2</sup> (Fig. 1c). This entails an equilibrium between the competing copper dissolution and the passivation reactions, slowing down the conversion of Cu to CuO.

The growth of NN structures depends on the electrolyte concentration as well as on the pH<sup>37</sup> while the use of  $c_{KOH} \ge$ 0.5 M is essential. The NN growth starts with a Cu2O layer, which, depending on the applied potential, (partially) dissolves to generate several nucleation sites. Anodization using potentials below the B<sub>1</sub> peak (0.75 V<sub>RHE</sub>) results in the growth of long NNs whose surface density increases with  $c_{KOH}$  as illustrated by the SEM image in Fig. 2a. The anodization potential just above the B1 peak (0.85 VRHE) or at the onset of the B2 peak produces densely packed shorter NNs. Once the applied anodization potential is close to the  $B_2$  peak (0.95  $V_{RHE}$ ), the NN growth is inhibited, as the reaction goes under the passivation regime control. The estimated depth of anodization related to the reconstruction of Cu<sub>300</sub> is calculated by integrating the current of the CA curves (Table S1†). Anodization depths of ~107, 83, 10 and 5 nm were estimated for AN-(0.75, 1), AN-(0.85, 0.5), AN-(0.95, 0.5) and AN-(0.75, 0.5), respectively (ESI S.2†).

The XRD patterns of the anodized electrodes are shown in Fig. 2b. The bare Cu<sub>300</sub> electrode has diffraction peaks at 43.3°, 50.4° and 74.1° which correspond to the (111), (200) and (220) planes of cubic fcc Cu (ICSD01-089-2838) shown by the rhombus symbol. The Cu thin film shows a (111)-preferred orientation. Additionally, the circle symbol is used for the peaks corresponding to the (111), (200), (220) planes of cubic Pt (ICSD01-087-0640) and observed at  $2\theta$  angles of 39.9°, 46.4°, and 67.4°, corresponding to the Pt layer supporting the sputtered copper film. The XRD peaks of the AN-(0.75, 0.5) and AN-(0.75, 1) samples located at 16.56°, 23.64°, 33.98°, 35.78°, 37.98°, 54.10°, and 63.52° correspond respectively to the (020), (021), (002), (111), (041), (061), and (200) planes of orthorhombic copper hydroxide Cu(OH)<sub>2</sub> (ICSD01-072-0140) as indicated by the heart symbol to indicate the presence of NNs. The lower intensity of these reflections in AN-(0.85, 0.5) suggests that a smaller amount and/or a less crystalline phase of Cu (OH)<sub>2</sub> is formed in this sample. In AN-(0.95, 0.5), only the Cu metal reflections corresponding to non-anodized substrate were observed suggesting that surface passivation has occurred impeding the formation of anodization products. The passivated area is either amorphous and/or of nanoscale dimension.

XPS of the Cu 2p core level was used to determine the initial surface oxidation state of the anodized Cu electrodes (Fig. 2c). The spin–orbit splitting of Cu 2p ( $\Delta$  = 19.75 eV) yields Cu 2p<sub>1/2</sub>: Cu 2p<sub>3/2</sub> components with an area ratio of 1:2. Our analysis is based on Cu 2p<sub>3/2</sub> where the peak at 932.6 eV is assigned to Cu<sup>+</sup>/Cu<sup>0</sup>, and peaks located close to the 933.5/934.5 eV (Cu<sup>2+</sup> region) stem from the Cu<sup>2+</sup> species in the oxide

Paper Nanoscale

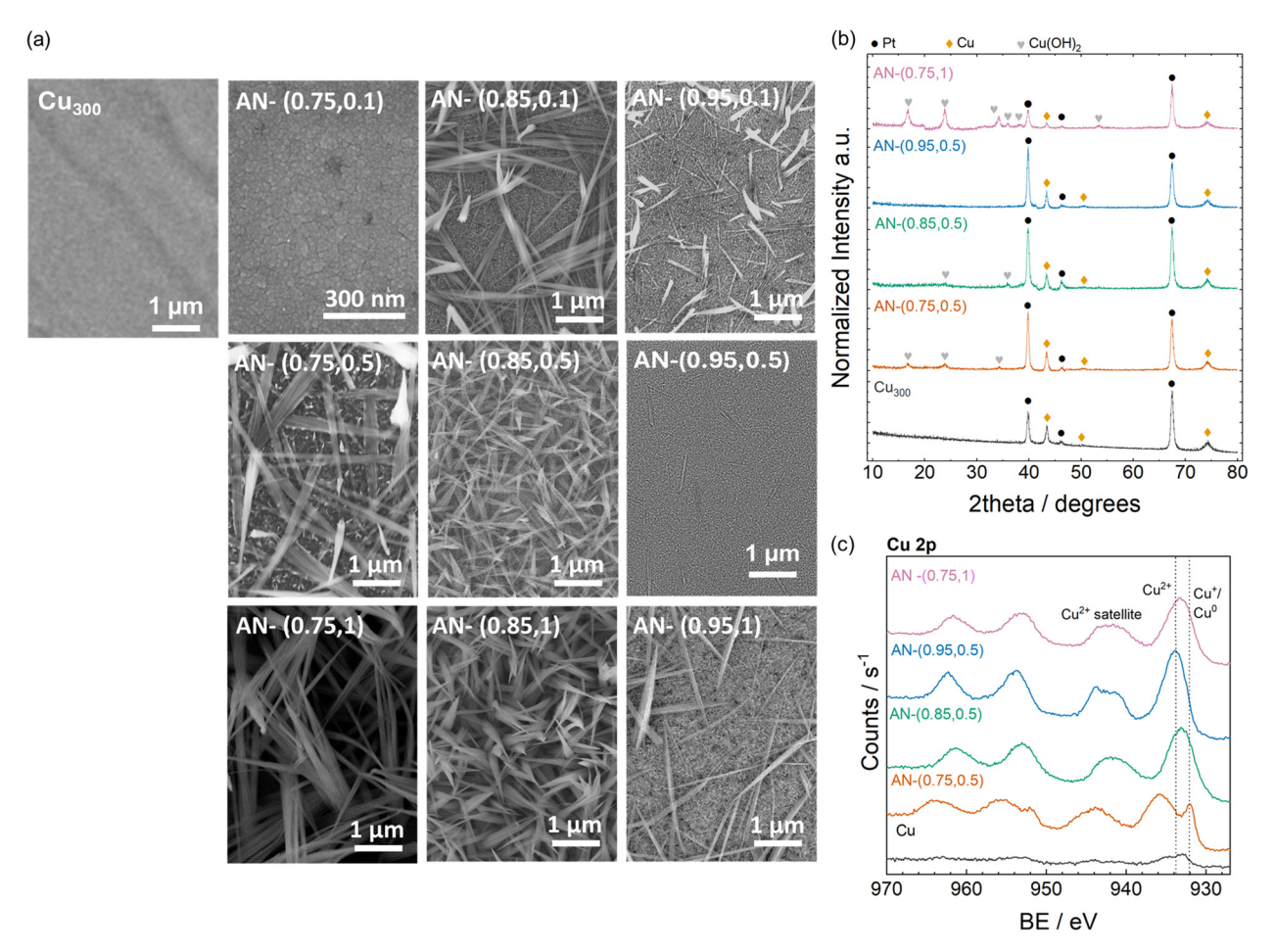


Fig. 2 Effects of anodization potential and KOH concentration in AN-(x, y): (a) surface morphology *via* SEM imaging *versus* the planar surface of Cu<sub>300</sub>. (b) crystallographic structure through XRD reflections. The rhombus symbol represents the characteristic cubic Cu planes (111), (200) and (220). The circle depicts the cubic Pt planes (111), (200) and (220), and the heart symbol shows the orthorhombic Cu(OH)<sub>2</sub> planes (020), (021), (002), (111), (041), (061), and (200), all in an ascending order of 2 theta, and (c) electronic structure from XPS Cu 2p core level spectra.

and hydroxide phases, respectively. The shape of the intense  $\mathrm{Cu}^{2+}$  satellite peaks appearing around 937–947 eV was qualitatively used to distinguish the hydroxide and oxide components.<sup>39</sup> Based on the satellite peak appearance, it can be concluded that  $\mathrm{Cu}^{2+}$  species are present in all the AN-(x, y) electrodes, agreeing with the expected oxidation state from Pourbaix diagrams<sup>40</sup> and the work of Stepniowski *et al.*<sup>41</sup>

The copper oxidation states can be further linked to the anodization parameters. Specifically, AN-(0.75, 0.5) consists of a mixture of  $Cu_2O$  and  $Cu^{2+}$  phases comprising Cu hydroxide as detected by XRD and possibly amorphous CuO. The  $Cu_2O$  phase is ascribed to the electrode's surface since the sample consists of sparse NNs (Fig. 2a); therefore its amount will be less than that of  $Cu^{2+}$ . Electrode AN-(0.85, 0.5) mainly consists of  $Cu^{2+}$ , Cu(OH)<sub>2</sub> as indicated by XRD. Unlike in the two previous electrodes, AN-(0.95, 0.5) surface appears to be fully oxidized into CuOas pointed out by the shape of the satellite peak and the absence of a hydroxide diffraction peaks. Although the hydroxide/oxide fraction cannot be precisely quantified, it is inferred that with a decreasing  $E_{an}$ , the hydroxide component systematically increases as does the density of NNs since they are largely composed of Cu hydroxide. Further confirmation of the prevalence of the Cu<sup>2+</sup> state in the form of CuO and Cu(OH)<sub>2</sub> phases is obtained from the Cu Auger LMM transition peak and the modified Auger parameter (Fig. S2 and Table S2†).

#### 3.3. Effect of NN morphology on the C<sub>2+</sub> selectivity

Fig. 3a shows the preliminary screening of the FE of the gaseous products formed under the  $CO_2RR$  at  $-1.0~V_{RHE}$  for the different AN-electrodes. Only gaseous products are shown since we are interested in ethylene production. Ethane, which is usually produced from porous electrodes, 42 was also detected but accounted for less than 1% of the total (Fig. S4b†). The missing FE values are of  $H_2$  and liquid products. Additional liquid product analysis quantified the presence of formic acid, ethanol, propanol, and acetaldehyde (vide infra). Variations in the FE follow changes in the geometrical current density, which is larger by a factor of about 2.2 for the NN-electrodes. Typical values for the NN-free electrodes are around  $-16~mA~cm^{-2}$  while those with NNs feature, depending on their morphology, current densities up to  $-33.5~mA~cm^{-2}$ .

(b) CH₄ [ 18 -35 16 0.95 Faradaic Efficiency / % 35 Anodization potential (V) 14 30 0.9 j / mA cm<sup>-2</sup> 25 0.85 10 15 0.8 0.75 0.250.51 0.85,0.5 0.95,0.5 10.75.0 \$85° 0.95,0,7 』 0.7 20 0.95 Anodization potential (V) (c) 0.9 C<sub>2+</sub>:C<sub>1</sub> ratio 0.85 0.8 0.75 0.7 0.2 0.4 0.6 0.8 1 KOH concentration (M) ПНСООН ПСН4  $C_2H_4$ @ -1.0 V<sub>RHE</sub> Faradaic Efficiency / % 60 50 -30 40 30 -25 20

Fig. 3 Electrochemical CO<sub>2</sub>RR performance of the AN-(x, y) electrode series: (a) CO<sub>2</sub>RR faradaic efficiency of gaseous products, CO, CH<sub>4</sub>, and C<sub>2</sub>H<sub>4</sub> and total current densities, (b) Contour plots derived from Fig. 3a showing the effect of the anodization process parameters on the CO<sub>2</sub>RR to  $CH_4$  (top) and  $C_2H_4$  (bottom), and (c) obtained total  $C_{2+}:C_1$  ratio. The ratio for \*Cu e-pol, refers to electropolished Cu, and is taken from ref. 38 (d) CO<sub>2</sub>RR faradaic efficiency of gaseous and liquid products and respective total current density of Cu<sub>300</sub>, AN-(0.75, 1) and AN-(250). Error bars represent the standard errors of the mean derived from three independent measurements; averages are plotted. The electrolysis experiments were held at a constant potential of -1.0 V<sub>RHE</sub> for 1 h.

AN-(0.75,1)

-20

10

Cu300

The contour plots shown in Fig. 3b reveal the variations in the FE for CH<sub>4</sub> and C<sub>2</sub>H<sub>4</sub> under the CO<sub>2</sub>RR with changes in the electrode morphology resulting from differences in the anodization conditions. Relating the CO2RR performance to the electrode morphology shows that CH<sub>4</sub> is the dominant CO<sub>2</sub>RR product in the absence of NNs. On the other hand, C<sub>2</sub>H<sub>4</sub> is favoured on electrodes featuring NNs. For the electrodes that produced the highest amount of C<sub>2</sub>H<sub>4</sub>, product selectivity was further quantified by the C2+: C1 ratio (C2+ products are ethylene, ethanol and propanol) in Fig. 3c whose maximization can be used as a criterion to select the electrode with the best performance. This ratio that equals 1.4 in the reference electropolished Cu foil38 increases by a factor of 2-3 in

the different anodized Cu thin films and reaches a maximum of  $\sim 6$  for AN-(0.75, 1).

Fig. 3d depicts the CO<sub>2</sub>RR FE of AN-(0.75, 1) versus that of the initial thin film Cu<sub>300</sub> and AN-(250), a new electrode with anodization time, which will be discussed later. Anodization of Cu<sub>300</sub> leads to a significant improvement in its C<sub>2+</sub> selectivity (Fig. 3d) that reaches 36% including  $FE_{C_2H_4}$  of 23%,  $FE_{EtOH}$  of 10% and FE<sub>PrOH</sub> of 3% while the FE for C<sub>1</sub> products is 6.2% including FE<sub>HCOOH</sub> of 4% and FE<sub>CH4</sub> of 1.6%. A minor amount of CO (< 0.5%) was detected which was not included in the C<sub>1</sub> products. This electrode reaches a partial geometric ethylene current density  $j_{C_2H_4}$  of -7.6 mA cm<sup>-2</sup> and a total geometric current density of -33.6 mA cm<sup>-2</sup>. The remaining current

limitations.

density is expected to participate in the competing  $H_2$  evolution reaction. This result is consistent with earlier works on nanoneedle-based electrodes that generally produce more  $C_{2+}$  over  $C_1$  products.  $^{8,19,29}$  In comparison, the original  $Cu_{300}$  thin film favours the production of  $C_1$  with a FE of 29.8% including  $FE_{CH_4}$  of 16.2%,  $FE_{HCOOH}$  of 12% and  $FE_{CO}$  of 1.6% while  $C_2$  only reaches 7.2% including  $FE_{C_2H_4}$  of 4.2% and  $FE_{EtOH}$  of 3%. Although relevant information regarding the relation between the NN morphology and the  $CO_2RR$  selectivity can be acquired in an H-cell, this configuration limits the FE towards  $C_2$  products compared to gas-fed flow cells due to the low solubility of  $CO_2$  in water, 0.034 M, resulting in mass transport

Since all electrodes have been measured in the same H-cell, differences in the selectivity are likely attributed to the morphology and the roughness (SRF) of their surface. To this end, the electrochemical surface area (ECSA) was estimated by performing CV in a suitable non-faradaic region (Fig. S5†).

The surface roughness factors (SRFs) of the as-prepared electrodes (Table S3†) increase sharply after the reaction likely due to the reconstruction process. The post-SRF rank is given in the following ascending order AN-(0.75, 0.5) < AN-(0.85, 0.5)< AN-(0.95, 0.5) < AN-(0.75, 1). However, an inverse order is revealed when the electrodes are compared according to their ECSA normalized current density,  $j_{ECSA}$  (Table S3†) with bare  $Cu_{300}$  showing a higher  $j_{ECSA}$  than AN-(0.75, 1). ECSA-normalized CO<sub>2</sub>RR activities of low and high surface area Cu catalysts generally depend on the conditions.<sup>43</sup> Higher ECSA leads to reactions that are more controlled from mass transport than from kinetics. Since rougher electrodes expose more active sites, they can deliver higher geometric currents that in turn increase the local pH.44,45 This pH increase can impede the selectivity of the CO2 reduction pathway toward pH-dependent products such as methane.46

The electrode that yields the highest  $C_{2+}$ :  $C_1$  ratio, AN-(0.75, 1), exhibits homogeneous high density and long NN features. It is also the electrode with the highest SRF. The increased length/tilting of the high curvature structure can suppress methane formation as proposed by Ma  $et~al.^{47}$  In our work, the formate production is reduced (corresponding  $FE_{C1}$  and  $FE_{C2+}$  can be found in Fig. S4c†). However, AN-(0.85, 0.5) and AN-(0.85, 1) that both feature shorter NNs compared to AN-(0.75, 1) feature similar  $FE_{C_2H_4}$  of 18% and 19.2%, respectively, compared to 23% in the latter electrode.

As a proof of concept, we further assessed the influence of the NN length by increasing the anodization time. With this objective, we made a new AN-(0.75, 1) electrode with prolonged anodization times from 150 to 250 s: AN-(250) where the value in brackets denotes the anodization time in s. Although this electrode shows an increased surface roughness (Fig. S5†), SEM imaging (Fig. S6b†) does not identify any apparent morphological differences from AN-(0.75, 1). No significant enhancement in  $\text{FE}_{\text{C}_2\text{H}_4}$  was observed while the current density only slightly increased from -33.6 to -35.1 mA cm<sup>-2</sup>. A stronger dependency of the  $\text{C}_{2+}$ :  $\text{C}_1$  ratio arises from the electrode SRF. It increases with SRF until it reaches a plateau suggesting

that mass transport may limit the reaction. Based on this, the SRF which is interconnected with the depth of NN formation and density, appears to have a larger impact on the ethylene/ $C_{2+}$  selectivity than on their length. The impact of the selected  $CO_2$  flow rate on the mass transport conditions was assessed by comparing the  $CO_2RR$  gas selectivity of the AN-(0.75,1) sample at 5 and 10 sccm. The  $CO_2$  flow rate was shown to only slightly affect the  $CO_2RR$  selectivity to gaseous products.

The importance of roughening Cu surface to steer its selectivity towards multicarbon species has been explored in recent AFM studies<sup>48</sup> as well as from the reduction of copper native oxides under the  $\rm CO_2RR.^{49}$  These morphological changes can form new under-coordinated and defective sites that may be active for C–C coupling. Another possible reason for the enhanced  $\rm C_{2+}$  selectivity on NNs is the increased bubble hydrodynamics, which enhances mass transport of products and reactants from and towards the electrode surface, respectively.<sup>50</sup>

#### 3.4. Reconstruction of NNs under the CO<sub>2</sub>RR

To gain better understanding of the correlation between the pre-reaction catalyst structure and its C2+ selectivity, we have investigated further the morphological evolution of the NN structure under the CO<sub>2</sub>RR and carried out post-reaction XAS and HAADF STEM for the best-performing AN-(0.15, 1) electrode. Reconstruction of copper electrocatalysts under the CO<sub>2</sub>RR has been demonstrated using in situ characterization techniques. For example, Lei et al. highlighted a correlation between grain size and C2+ selectivity on reduced oxide-derived Cu nanocrystals, peaking with 11 nm.<sup>51</sup> In another operando STEM study, the size of nanograins formed through the agglomeration of 5-7 nm Cu nanoparticles (NPs), is evidenced to control the CO2RR product selectivity because of their ability to form higher density metallic Cu grains. 16 Those earlier results suggest that controlling the size of the Cu NPs via the anodization of the electrode may allow tuning the selectivity towards C2 productivity.

The relative preservation of the NN shape observed by postreaction SEM enables us to acquire meaningful structural information of our catalysts despite their air exposure between the characterization measurements. Specifically, the SEM image of post-reaction AN-(0.75, 1)-CO<sub>2</sub>RR in Fig. 4a shows that although the aspect of the NNs is roughened they retain their original shape. Similar reconstruction of copper electrodes during the CO<sub>2</sub>RR has been ascribed previously to the dissolution and redeposition of Cu under negative applied potentials.<sup>52</sup>

The XANES spectra in Fig. 4b provide information on the copper local electronic structure in AN-(0.75, 1) prior and after the CO<sub>2</sub>RR by using reference compounds as standards. The absorption edge shift increases with increasing oxidation state. As expected, the initial pre-reaction profile of AN-(0.75, 1) consists of a mixture of oxides (Cu<sub>2</sub>O, CuO/Cu(OH)<sub>2</sub>). Their post-reaction profile matches that of the Cu foil and the initial sputtered Cu electrode. This shows that the largely oxidized

(b) (C) 35 - Cu K-edge AN-(0.75,1) AN-(0.75,1)-CO2RR Normalized xµ(E) 30 Cu<sub>300</sub> FT k $^2\chi$ (k) / Å $^4$ 25 20 Cu-C 10 AN-(0.75,1) - - - CuO ref. AN-(0.75,1)-CO2RR ----- Cu2O ref. 5 ---- Cu ref. Cu<sub>300</sub> 9000 8975 9025 9050 R/Å Energy / eV (e) (d)002 50 nm 200 nm (f)

Fig. 4 (a) SEM image of AN-(0.75, 1)-CO<sub>2</sub>RR. Cu K-edge XANES (b) and EXAFS (c) spectra of AN-(0.75, 1) before and after the CO<sub>2</sub>RR, along with the Cu<sub>300</sub> substrate and Cu foil, Cu<sub>2</sub>O and CuO reference spectra. HAADF STEM image of the (d) initial NN and high-resolution image of the NN broken tip indicated by the red square. The FFT pattern inset shows the zone axis and the crystalline planes of the crystal structures in the green dashed square, confirming the orthorhombic structure (space group: Cmca) of Cu(OH)<sub>2</sub>. (e) NN after the CO<sub>2</sub>RR and high-resolution image of the NN edge indicated by the blue square. FFT pattern insets of the crystal structures in the orange and maroon dashed squares, confirming the cubic structure (space group:  $Fm\bar{3}m$ ) of Cu<sub>2</sub>O, respectively. (f) TEM lamella of the as-prepared NNs and high-resolution image indicated by the orange square, revealing its microstructure with large nanoparticles at the core and smaller nanoparticles surrounding them. (g) TEM lamella of NNs after the CO<sub>2</sub>RR, showing enlarged core nanoparticles and the high-resolution image of the large surface particles with smaller nanoparticles below them, indicated by the purple square.

structure of AN-(0.75, 1) is reduced into metallic Cu during the  $CO_2RR$  and remains so under the ambient conditions.

The EXAFS fitting results reflecting the copper atoms local environment are summarized in Table S4.† Fourier transforms (FTs) of  $k^2$ -weighted EXAFS in Fig. 4c show two peaks at 1.9 Å and 2.5 Å corresponding to Cu–O and Cu–Cu contributions, respectively in the as-prepared AN-(0.75, 1) while post CO<sub>2</sub>RR, only a very intense Cu–Cu peak remains. Before the CO<sub>2</sub>RR, copper atoms in AN-(0.75, 1) are surrounded by 2.4 O at 1.93 Å and 3.7 Cu at 2.54 Å corresponding to a copper oxide and copper metal shell, respectively. The metal shell accounts for the remaining part of the Cu layer that was not anodized beneath the NN. The fractions of the different copper oxides calculated using a simple combination of the coordination numbers

and bond distances was ca. 30% of  $Cu_2O$  and ca. 70% of  $Cu^{2+}$  (ESI S.7†).

In post-reaction AN-(0.75, 1)-CO<sub>2</sub>RR Cu atoms are surrounded by 0.3 O at 1.85 Å corresponding to ca. 15% of Cu<sub>2</sub>O phase and 85% of Cu metal with 8.5 Cu at 2.53 Å (ESI S.7†). The corrected average coordination number ( $N_{\rm Cu,r}$ ) of Cu metal was found to be 10.0 (8.5/0.85) with a crystallite size of ca. 2.3 nm (Table S5†). From the TEM lamella image after the CO<sub>2</sub>RR, we notice that the initial sputtered layer is no longer observed post-reaction, implying that the small crystallite size exclusively coincides with the reconstructed NNs during the CO<sub>2</sub>RR. The whole electrode comprising the non-anodized thin film and the NNs might reconstruct upon application of very negative potential.<sup>53</sup> The original Cu<sub>300</sub> whose EXAFS

could be fitted with 0.2 O at 1.86 Å and 10.5 (11.7) Cu at 2.54 Å

corresponds to ca. 10% of Cu<sub>2</sub>O and ca. 90% of Cu<sup>0</sup> with an average crystallite size of ca. 16 nm in line with the particle size of ca. 20 nm obtained with XRD (Table S6†).

HAADF STEM was used to image the structure of the NN in AN-(0.75, 1). The results show that the as-prepared NNs consist of relatively smooth and uniform long fibres as shown in the HAADF STEM image of an individual NN in Fig. 4d. The corresponding Fast Fourier Transform (FFT) agrees well with the orthorhombic structure (space group: Cmca) of Cu(OH)<sub>2</sub>.<sup>54</sup> The high-resolution HAADF STEM image of a TEM lamella prepared from the sample reveals a microstructure composed of small nanoparticles with an average size of 2.11  $\pm$  0.10 nm (Fig. 4f). Additionally, this cross-sectional analysis shows the formation of a compact polycrystalline copper core within the NNs as shown in Fig. 4f and g and the EDS analysis for this area is shown in Fig. S9.† In as-prepared AN-(0.75, 1), this copper core may consist of Cu hydroxide crystallites of up to 12 nm as detected by XRD (Table S6†).

For AN-(0.75, 1)-CO<sub>2</sub>RR, the HAADF STEM image in Fig. 4d shows that the NNs undergo structural and surface morphological changes, including surface roughening. FFT analysis confirms the presence of the cubic structure (space group:  $Fm\bar{3}m$ ) of Cu metal<sup>55</sup> and Cu<sub>2</sub>O (space group: Pn3m).<sup>56</sup> Moreover, a change in the averaged atomic ratio of Cu:O from 1:1 in the as-prepared NNs to 9:1 after CO2RR is observed. As EXAFS pointed out the reduction of copper to a metallic state, the latter ratio indicates that this small oxygen content is likely resulting from air exposure of the samples between the measurements, as it is detected mostly on the surface (Fig. S8 and Table S8†). Highresolution HAADF STEM of the sample TEM lamella reveals enlarged surface particles with average sizes of 5.77 ± 1.83 nm, while smaller nanoparticles of 2.01 ± 0.14 nm remain beneath the surface (Fig. 4f). The top layer consists of smaller Pt NPs deposited during the FIB process for sample protection as confirmed by the EDS maps of the TEM lamella (Fig. S9†).

During anodization, Cu<sub>300</sub> is transformed according to the conditions up to a specific depth into NNs in the form of a Cu(OH)<sub>2</sub> phase. However, the remaining copper film might participate in the reaction only if CO2 can diffuse to this NN depth.<sup>57</sup> This follows the selectivity trend of the AN-(0.75, 1) electrode, where inhomogeneous NN coverage leads to a significant decrease in  $C_{2+}$  or  $C_2H_4$  production. The  $Cu(OH)_2$  NPs forming the NNs in AN-(0.75, 1) reassemble into slightly bigger Cu metal NPs of 5 nm in AN-(0.75, 1)-CO<sub>2</sub>RR while their polycrystalline domains show a size of 2.3 nm. Our results are in agreement with those of Lei et al., which point to the presence of small Cu nanograins after the CO2RR either in a heatquench or anodized Cu surface.<sup>29</sup> However, our samples show the occurrence of an even smaller crystal size after the CO<sub>2</sub>RR.

The NN inner structure reveals that a 3D-network consisting of 2 nm Cu(OH)<sub>2</sub> NPs created earlier at the anodization stage is reduced to a 5 nm metallic Cu NP network during the CO2RR. This is supported by the dynamic transformation of catalytically inactive single Cu atoms<sup>58</sup> into C<sub>2</sub> active-metal nanoparticles. Based on previous works, it is our hypothesis that

these porous Cu NP networks efficiently trap CO2 and CO2RR gaseous intermediates in between of NNs59 or inside their porous structure,60 resulting in an increase of the number of available active sites but also of the local CO concentration.<sup>61</sup> In addition, C-C coupling is proposed to be more favourable in these NN strucures. 47 Our results suggest that a catalyst surface with a high metallic character is needed to allow the formation of C2+ molecules. This would also agree with the demonstrated NN tip-induced amplified electric field attracting more hydrated K<sup>+</sup> cations as shown for CO electroreduction.<sup>62</sup> A high density of NNs featuring similar inner structures is likely the most important parameter controlling the C<sub>2+</sub> production.

Utilization of thin film electrodes in scaled-up CO<sub>2</sub> electrolyzers can be envisaged as the anodization process can be ideally applied to the fabrication of gas diffusion electrodes (GDEs) with larger surface areas and higher gas permeation. As zero-gap electrolyzers typically operate with concentrated KOH electrolyte, the initial anodization of the Cu thin films by applying an oxidative current density prior to the CO<sub>2</sub>RR would conveniently produce high density NN surfaces. However, testing the long-term performance of these catalysts under industrial conditions would be required for their future application. According to Yu et al.,63 the continuous agglomeration of metallic NPs that may occur during prolonged operation could lower the C<sub>2+</sub> selectivity of the copper catalysts, leading to their deactivation. Improving the existing electrode configuration by adding an additional layer of a different metal to produce a tandem catalyst<sup>64</sup> is also a promising strategy to fully utilize the potential of NNs.

## Conclusions

In conclusion, the influence of  $E_{\rm an}$  and  $c_{\rm KOH}$  anodization parameters on tailoring the density and length of Cu(OH)2/CuO NNs grown on sputtered Cu films was investigated. Their CO<sub>2</sub>RR performance in terms of C<sub>2+</sub>: C<sub>1</sub> ratio measured in a H-cell surpassed that of bare Cu<sub>300</sub>, with AN-(0.75, 1) ratio featuring a nearly 20-fold increase relative to that of the bare film at a fixed potential of -1.0 V<sub>RHE</sub>. Our results showed that a high SRF and NN density is required to reach a high C2H4 (or C<sub>2+</sub>) selectivity. More importantly, post-reaction-microscopy and XAFS investigations highlight that the NNs consist of a very small porous 3D network with metallic Cu NPs. The high density of NNs with a similar inner porous structure trait is likely to increase their C2+ selectivity. Based on our comprehensive study, we present a relationship between the NN features and their inner structure on the selectivity of the CO<sub>2</sub>RR, providing a better understanding of the nanostructuring process of copper thin film electrocatalysts.

### **Author contributions**

D. P.: writing - original draft, conceptualization, investigation, formal analysis, and visualization; F. F.: methodology, visualNanoscale Paper

ization, and writing – review and editing; D. B.: investigation and writing – review and editing; I. A.: investigation and writing – review and editing; T. N.: writing – review and editing; D. P., S. B. and I. T.: writing – review and editing, and resources; D. G., E. J. and P. L.: writing – review and editing, project administration, and funding acquisition.

## Conflicts of interest

There are no conflicts to declare.

## Data availability

The data of this article are shown in the figures and the ESI.†

The raw data shown in the figures are available on the KU

Leuven institutional research data repository at https://doi.org/
10.48804/I6WO1U.

## Acknowledgements

This work was supported by the European Union under the MSCA Innovative Training Network CATCHY (grant agreement no. 955650) and by the Flanders Innovation & Entrepreneurship (VLAIO) project HBC.2021.0586 (CLUE). T.H.T. Nguyen thanks the Research Foundation Flanders (FWO) for a FWO MSCA SoE postdoctoral fellowship (12ZZI.23N). Filippo Franceschini acknowledges the support of the Research Foundation Flanders (FWO) for the PhD fellowship (1S61725N).

Access to Elettra synchrotron was provided by the European the Horizon Europe Union part of HORIZON-INFRA-2021-SERV-01 under grant agreement number 101058414 and co-funded by UK Research and Innovation (UKRI) under the UK government's Horizon Europe funding guarantee (grant number 10039728) and by the Swiss State Secretariat for Education, Research and Innovation (SERI) under contract number 22.00187: 'Views and opinions expressed are however those of the author(s) only and do not necessarily reflect those of the European Union or the UK Science and Technology Facilities Council or the Swiss State Secretariat for Education, Research and Innovation (SERI). Neither the European Union nor the granting authorities can be held responsible for them.

Finally, we would like to thank Luca Olivi and the staff of the XAFS beamline at Elettra synchrotron for providing guidance and assistance. We would also like to thank Zviadi Zarkua for his assistance and discussions on XPS data.

#### References

 I. E. L. Stephens, K. Chan, A. Bagger, S. W. Boettcher, J. Bonin, E. Boutin, A. K. Buckley, R. Buonsanti, E. R. Cave, X. Chang, S. W. Chee, A. H. M. Da Silva, P. De Luna, O. Einsle, B. Endrődi, M. Escudero-Escribano, J. V. Ferreira

- De Araujo, M. C. Figueiredo, C. Hahn, K. U. Hansen, S. Haussener, S. Hunegnaw, Z. Huo, Y. J. Hwang, C. Janáky, B. S. Jayathilake, F. Jiao, Z. P. Jovanov, P. Karimi, M. T. M. Koper, K. P. Kuhl, W. H. Lee, Z. Liang, X. Liu, S. Ma, M. Ma, H.-S. Oh, M. Robert, B. R. Cuenya, J. Rossmeisl, C. Roy, M. P. Ryan, E. H. Sargent, P. Sebastián-Pascual, B. Seger, L. Steier, P. Strasser, A. S. Varela, R. E. Vos, X. Wang, B. Xu, H. Yadegari and Y. Zhou, *J. Phys.: Energy*, 2022, 4, 042003.
- 2 Y. Y. Birdja, E. Pérez-Gallent, M. C. Figueiredo, A. J. Göttle, F. Calle-Vallejo and M. T. M. Koper, *Nat. Energy*, 2019, 4, 732–745.
- 3 D. Xu, K. Li, B. Jia, W. Sun, W. Zhang, X. Liu and T. Ma, *Carbon Energy*, 2023, 5, e230.
- 4 O. S. Bushuyev, P. De Luna, C. T. Dinh, L. Tao, G. Saur, J. Van De Lagemaat, S. O. Kelley and E. H. Sargent, *Joule*, 2018, 2, 825–832.
- 5 A. Bagger, W. Ju, A. S. Varela, P. Strasser and J. Rossmeisl, *ChemPhysChem*, 2017, **18**, 3266–3273.
- 6 S. Nitopi, E. Bertheussen, S. B. Scott, X. Liu, A. K. Engstfeld, S. Horch, B. Seger, I. E. L. Stephens, K. Chan, C. Hahn, J. K. Nørskov, T. F. Jaramillo and I. Chorkendorff, *Chem. Rev.*, 2019, 119, 7610–7672.
- 7 C. Zhan, F. Dattila, C. Rettenmaier, A. Herzog, M. Herran, T. Wagner, F. Scholten, A. Bergmann, N. López and B. Roldan Cuenya, *Nat. Energy*, 2024, 9, 1485–1496.
- 8 S. Y. Lee, H. Jung, N.-K. Kim, H.-S. Oh, B. K. Min and Y. J. Hwang, *J. Am. Chem. Soc.*, 2018, **140**, 8681–8689.
- 9 T. Saberi Safaei, A. Mepham, X. Zheng, Y. Pang, C.-T. Dinh, M. Liu, D. Sinton, S. O. Kelley and E. H. Sargent, *Nano Lett.*, 2016, 16, 7224–7228.
- 10 M. C. O. Monteiro, F. Dattila, B. Hagedoorn, R. García-Muelas, N. López and M. T. M. Koper, *Nat. Catal.*, 2021, 4, 654–662.
- 11 H. Mistry, A. S. Varela, C. S. Bonifacio, I. Zegkinoglou, I. Sinev, Y.-W. Choi, K. Kisslinger, E. A. Stach, J. C. Yang, P. Strasser and B. R. Cuenya, *Nat. Commun.*, 2016, 7, 12123.
- 12 J.-J. Velasco-Vélez, T. Jones, D. Gao, E. Carbonio, R. Arrigo, C.-J. Hsu, Y.-C. Huang, C.-L. Dong, J.-M. Chen, J.-F. Lee, P. Strasser, B. Roldan Cuenya, R. Schlögl, A. Knop-Gericke and C.-H. Chuang, ACS Sustainable Chem. Eng., 2019, 7, 1485–1492.
- 13 M. Favaro, H. Xiao, T. Cheng, W. A. Goddard, J. Yano and E. J. Crumlin, *Proc. Natl. Acad. Sci. U. S. A.*, 2017, **114**, 6706–6711.
- 14 A. Eilert, F. Cavalca, F. S. Roberts, J. Osterwalder, C. Liu, M. Favaro, E. J. Crumlin, H. Ogasawara, D. Friebel, L. G. M. Pettersson and A. Nilsson, *J. Phys. Chem. Lett.*, 2017, 8, 285–290.
- 15 P. De Luna, R. Quintero-Bermudez, C.-T. Dinh, M. B. Ross, O. S. Bushuyev, P. Todorović, T. Regier, S. O. Kelley, P. Yang and E. H. Sargent, *Nat. Catal.*, 2018, 1, 103–110.
- 16 Y. Yang, S. Louisia, S. Yu, J. Jin, I. Roh, C. Chen, M. V. Fonseca Guzman, J. Feijóo, P.-C. Chen, H. Wang, C. J. Pollock, X. Huang, Y.-T. Shao, C. Wang, D. A. Muller, H. D. Abruña and P. Yang, *Nature*, 2023, 614, 262–269.

17 M. Löffler, K. J. J. Mayrhofer and I. Katsounaros, *J. Phys. Chem. C*, 2021, 125, 1833–1838.

- 18 J. Timoshenko, A. Bergmann, C. Rettenmaier, A. Herzog, R. M. Arán-Ais, H. S. Jeon, F. T. Haase, U. Hejral, P. Grosse, S. Kühl, E. M. Davis, J. Tian, O. Magnussen and B. Roldan Cuenya, *Nat. Catal.*, 2022, 5, 259–267.
- 19 M. Ma, K. Djanashvili and W. A. Smith, *Angew. Chem., Int. Ed.*, 2016, 55, 6680–6684.
- 20 W. J. Stępniowski, H. Yoo, J. Choi, P. Chilimoniuk, K. Karczewski and T. Czujko, Surf. Interfaces, 2019, 14, 15– 18.
- 21 J. Ambrose, R. G. Barradas and D. W. Shoesmith, J. Electroanal. Chem. Interfacial Electrochem., 1973, 47, 47–64.
- 22 A. Brudzisz, D. Giziński, M. Liszewska, E. Wierzbicka, U. Tiringer, S. A. Taha, M. Zając, S. Orzechowska, B. Jankiewicz, P. Taheri and W. J. Stępniowski, *Electrochim. Acta*, 2023, 443, 141918.
- 23 R. Garg, S. Gonuguntla, S. Sk, M. S. Iqbal, A. O. Dada, U. Pal and M. Ahmadipour, Adv. Colloid Interface Sci., 2024, 330, 103203.
- 24 N. S. Gultom, Q. Ha, M. Z. Silitonga and D. Kuo, *ChemCatChem*, 2024, **16**, e202301312.
- 25 B. Barbee, B. Muchharla, A. Adedeji, A. Karoui, K. Kumar Sadasivuni, M. S. Sha, A. M. Abdullah, G. Slaughter and B. Kumar, Sci. Rep., 2022, 12, 7507.
- 26 M. S. Abdel-wahab, H. K. E. Emam and W. M. A. E. Rouby, *RSC Adv.*, 2023, **13**, 10818–10829.
- 27 D. W. Shoesmith, T. E. Rummery, D. Owen and W. Lee, J. Electrochem. Soc., 1976, 123, 790.
- 28 W. J. Stępniowski, D. Paliwoda, S. T. Abrahami, M. Michalska-Domańska, K. Landskron, J. G. Buijnsters, J. M. C. Mol, H. Terryn and W. Z. Misiolek, *J. Electroanal. Chem.*, 2020, 857, 113628.
- 29 Q. Lei, H. Zhu, K. Song, N. Wei, L. Liu, D. Zhang, J. Yin, X. Dong, K. Yao, N. Wang, X. Li, B. Davaasuren, J. Wang and Y. Han, J. Am. Chem. Soc., 2020, 142, 4213–4222.
- 30 G. Iijima, T. Inomata, H. Yamaguchi, M. Ito and H. Masuda, *ACS Catal.*, 2019, **9**, 6305–6319.
- 31 F. Franceschini, C. Fernandes, K. Schouteden, J. Ustarroz, J. P. Locquet and I. Taurino, *Catal. Sci. Technol.*, 2025, **15**, 3022–3035.
- 32 A. D. Cicco, G. Aquilanti, M. Minicucci, E. Principi, N. Novello, A. Cognigni and L. Olivi, *J. Phys.: Conf. Ser.*, 2009, **190**, 012043.
- 33 S. D. Giri and A. Sarkar, *J. Electrochem. Soc.*, 2016, **163**, H252–H259.
- 34 D. W. Shoesmith, J. Electroanal. Chem., 1983, 143, 153-165.
- 35 I. Platzman, R. Brener, H. Haick and R. Tannenbaum, J. Phys. Chem. C, 2008, 112, 1101–1108.
- 36 X. Wu, H. Bai, J. Zhang, F. Chen and G. Shi, *J. Phys. Chem. B*, 2005, **109**, 22836–22842.
- 37 S. Anantharaj, H. Sugime, S. Yamaoka and S. Noda, *ACS Appl. Energy Mater.*, 2021, 4, 899–912.
- 38 K. P. Kuhl, E. R. Cave, D. N. Abram and T. F. Jaramillo, *Energy Environ. Sci.*, 2012, 5, 7050.

- 39 M. C. Biesinger, Surf. Interface Anal., 2017, 49, 1325-1334.
- 40 M. Pourbaix, Corros. Sci., 1974, 14, 25-82.
- 41 W. Stepniowski and W. Misiolek, *Nanomaterials*, 2018, 8, 379.
- 42 R. Kas, R. Kortlever, H. Yılmaz, M. T. M. Koper and G. Mul, *ChemElectroChem*, 2015, 2, 354–358.
- 43 E. L. Clark, J. Resasco, A. Landers, J. Lin, L.-T. Chung, A. Walton, C. Hahn, T. F. Jaramillo and A. T. Bell, ACS Catal., 2018, 8, 6560–6570.
- 44 Y. Pang, T. Burdyny, C.-T. Dinh, M. G. Kibria, J. Z. Fan, M. Liu, E. H. Sargent and D. Sinton, *Green Chem.*, 2017, 19, 4023–4030.
- 45 M. C. O. Monteiro, A. Mirabal, L. Jacobse, K. Doblhoff-Dier, S. C. Barton and M. T. M. Koper, *JACS Au*, 2021, 1, 1915– 1924.
- 46 E. L. Clark and A. T. Bell, J.Am. Chem. Soc., 2018, 140, 7012–7020.
- 47 M. Ma, K. Djanashvili and W. A. Smith, *Angew. Chem., Int. Ed.*, 2016, 55, 6680–6684.
- 48 K.-L. C. Nguyen, J. P. Bruce, A. Yoon, J. J. Navarro, F. Scholten, F. Landwehr, C. Rettenmaier, M. Heyde and B. R. Cuenya, *ACS Energy Lett.*, 2024, **9**, 644–652.
- 49 S. J. Raaijman, N. Arulmozhi and M. T. M. Koper, *ACS Appl. Mater. Interfaces*, 2021, 13, 48730–48744.
- 50 T. Burdyny, P. J. Graham, Y. Pang, C.-T. Dinh, M. Liu, E. H. Sargent and D. Sinton, *ACS Sustainable Chem. Eng.*, 2017, 5, 4031–4040.
- 51 Q. Lei, L. Huang, J. Yin, B. Davaasuren, Y. Yuan, X. Dong, Z.-P. Wu, X. Wang, K. X. Yao, X. Lu and Y. Han, *Nat. Commun.*, 2022, 13, 4857.
- 52 J. Vavra, G. P. L. Ramona, F. Dattila, A. Kormányos, T. Priamushko, P. P. Albertini, A. Loiudice, S. Cherevko, N. Lopéz and R. Buonsanti, *Nat. Catal.*, 2024, 7, 89–97.
- 53 P. Wilde, P. B. O'Mara, J. R. C. Junqueira, T. Tarnev, T. M. Benedetti, C. Andronescu, Y. T. Chen, R. D. Tilley, W. Schuhmann and J. J. Gooding, *Chem. Sci.*, 2021, 12, 4028–4033.
- 54 H. R. Oswald, A. Reller, H. W. Schmalle and E. Dubler, *Acta Crystallogr., Sect. C:Cryst. Struct. Commun.*, 1990, **46**, 2279–2284. Accessed from <a href="https://www.crystallography.net/cod/9007849.html">https://www.crystallography.net/cod/9007849.html</a> on 26 June 2024.
- 55 A. D. Fortes, M. H. Lemée-Cailleau, C. J. Pickard and R. J. Needs, J. Am. Chem. Soc., 2009, 131, 13508–13515.
- 56 A. Kirfel and K. Eichhorn, *Acta Crystallogr., Sect. A:Found. Crystallogr.*, 1990, **46**, 241–284. Accessed from <a href="https://www.crystallography.net/cod/1000063.html">https://www.crystallography.net/cod/1000063.html</a> on 26 June 2024.
- 57 C. T. Dinh, T. Burdyny, M. G. Kibria, A. Seifitokaldani, C. M. Gabardo, F. P. García De Arquer, A. Kiani, J. P. Edwards, P. De Luna, O. S. Bushuyev, C. Zou, R. Quintero-Bermudez, Y. Pang, D. Sinton and E. H. Sargent, *Science*, 2018, 360, 783–787.
- 58 J. Zhang, T. H. My Pham, Z. Gao, M. Li, Y. Ko, L. Lombardo, W. Zhao, W. Luo and A. Züttel, *ACS Catal.*, 2023, 13, 9326–9335.
- 59 A. Dutta, M. Rahaman, N. C. Luedi, M. Mohos and P. Broekmann, *ACS Catal.*, 2016, **6**, 3804–3814.

- 60 J. R. C. Junqueira, P. B. O'Mara, P. Wilde, S. Dieckhöfer, T. M. Benedetti, C. Andronescu, R. D. Tilley, J. J. Gooding and W. Schuhmann, *ChemElectroChem*, 2021, 8, 4848–4853.
- 61 S. Louisia, D. Kim, Y. Li, M. Gao, S. Yu, I. Roh and P. Yang, *Proc. Natl. Acad. Sci. U. S. A.*, 2022, **119**, e2201922119.
- 62 W. Ren, H. Zhang, M. Chang, N. Chen, W. Ma, J. Gu, M. Lin and X. Hu, *Chem*, 2025, 11, 102352.
- 63 J. Yu, Y. Zheng, B. Lv, A. Huang, J. Zhang, Z. Wang, Y. Zhang, Y. Wu, Y. Zhou, Y. Wang and W. Luo, *Appl. Catal. B: Environ.*, 2025, 368, 125131.
- 64 L. Bian, Y. Bai, J.-Y. Chen, H.-K. Guo, S. Liu, H. Tian, N. Tian and Z.-L. Wang, *ACS Nano*, 2025, **19**, 9304–9316.